

Representation of topography by porous barriers and objective interpolation of topographic data

Alistair Adcroft

Program in Atmospheric and Oceanic Sciences, Princeton University, 300 Forrestal Rd., Sayre Hall, Princeton, NJ 08540-6654, United States

ARTICLE INFO

Article history:

Received 5 November 2012

Received in revised form 8 February 2013

Accepted 11 March 2013

Available online 29 March 2013

Keywords:

Topography

Objective interpolation

Cut-cells

Finite volume

Tsunami

Overflow

ABSTRACT

We present a porous medium approach to representing topography, and a new algorithm for the objective interpolation of topography, for use in ocean circulation models of fixed resolution. The representation and algorithm makes use of two concepts; impermeable thin walls and porous barriers. Impermeable thin walls allow the representation of knife-edge sub-grid-scale barriers that block lateral flow between model grid cells. Porous barriers permit the sub-grid scale geometry to modulate lateral transport as a function of elevation. We find that the porous representation and the resulting interpolated topography retains key features, such as overflow sill depths, without compromising other dynamically relevant aspects, such as mean ocean depth for a cell. The accurate representation of the ocean depth is illustrated in a simple model of a tsunami that has a cross-basin travel time very much less dependent on horizontal resolution than when using conventional topographic interpolation and representation.

© 2013 Elsevier Ltd. All rights reserved.

1. Introduction

One of the physical characteristics that distinguishes the ocean from the atmosphere is the presence of topography that varies on the scale of the depth of the fluid. Ocean circulation models have always had to contend with side-walls and coast-lines which can be challenging to represent faithfully from a geographic perspective. For instance, in global ocean circulation models, the position of a coastline is often displaced to a model grid-line or a topographic slope is misrepresented due to lack of horizontal resolution. Further, the leading order topographic variations themselves lead to circulation structures that either need to be resolved (e.g. boundary currents, coastal upwelling) or lead to small-scale processes (unresolved) that should be parametrized (e.g. standing eddies, mixing by breaking internal waves, etc.).

Typically, and particularly at coarser horizontal resolutions (e.g. >100 km), the model topography is almost always a compromise between some objectively generated topography and a more subjective process involving some user intervention. The intervention is required to retain or restore geographic features of importance which the objective algorithm filtered. For instance, if we use sub-sampling or spatial averaging to objectively map a high-resolution topographic data set to a 1° global grid, the Isthmus of Panama might become flooded and the Straits of Gibraltar might become closed, depending on the particular choice of horizontal

grid and algorithm. Connectivity issues that arise from these adjustments of coastlines are fairly easy to recognize by eye, due to our familiarity with, and the availability of, maps of the world. Less obvious to detect are sub-surface discrepancies such as the depth of a sill, or the height of abyssal barriers, with which we are less familiar and expert at recognizing by eye, and for which there is only imperfect data; we all recognize a map of coastlines but are less likely to notice a missing saddle in a 1000 meter isobath. Fortunately, observational oceanography has identified many key topographic features, with associated processes such as hydraulic control at overflow sites (Price and Baringer, 1994) or mixing in fracture zones (Ferron et al., 1998), that are important in shaping the water-masses and pathways in the ocean. These provide a list of features that can be checked and corrected by human intervention. Unfortunately, documenting the editing of model topography is time consuming, often overlooked, or not published, all of which essentially leads to non-reproducible results.

When topography generation requires user intervention we consider the process potentially subjective for two reasons: i) the decision as to how to edit the topography is inherently subjective (one of multiple data points might be raised to block Panama but which is best?), and ii) the list of relevant known key topographic features is finitely small, probably incomplete and primarily relevant to large scale oceanography. The fractal and multi-scale nature of topography means that there are probably many unnamed topographic features that play an important role in local dynamics

E-mail address: aadcroft@princeton.edu

(e.g. Taylor caps, spill jets (Magaldi et al., 2011)) that will go uncorrected.

In the last decade, the horizontal resolution of bathymetry data has improved greatly; early global datasets were a blend of many alternate data sources, with irregular and sparse coverage, inconsistent calibrations and many bad or contradictory measurements. Recent gravitational data (Smith and Sandwell, 1997) has provided a significantly more uniform treatment of topography. The modern datasets have led to previously unknown features (Sandwell and Wessel, 2010) and eliminated formerly imaginary ones, e.g., a chain of 3000 m tall sea mounts at 66°S, 24°W that disappeared from the ETOPO gridded datasets between the 5' and 2' products (NGDC, 2006). The newer gridded data are still imperfect in two ways: first, the data is often modelled or objectively interpolated and may not be validated by direct measurements. Second, information is lost during the act of gridding to a particular resolution because the sub-grid scale variations are necessarily not representable. In contemporary data sets, the data might be defined (or interpreted) to be the mean or median height of the grid cell and features shorter than the grid are unrecoverable. For example, the Bosphorus is closed in the Smith and Sandwell (1997) dataset and yet we know that within a 1' by 1' cell there is channel that should connect the Black Sea to the Sea of Marmara.

High-resolution topographic data is typically interpreted as cell averages on the original grid for no reason other than that is what ocean models are built to use on the coarse grid.¹ The direct numerical representation of topography in a model might be via some high order method (see the discussion on cut-cells later) but the topography is considered to be resolved by the grid. That is to say, from the cell mean data on a coarse grid, the best a model can do is fit curves (or by some other means) to obtain smoother or more accurate representation of a resolvable boundary shape.

Here, we propose that a representation of sub-grid scale topography can modulate the resolved model transport and evolution, even with only one degree of freedom per cell for state variables. The method we propose is not unlike a porous media approach but we present it as a natural extension of the finite volume formulation introduced in Adcroft et al. (1997). To do so, we discuss two concepts for representing topography in ocean models: impermeable thin walls and porous barriers. Thin walls allow the separation of topography into column data and edge data. Impermeable thin walls define an absolute connectivity of model columns on a finite resolution grid. Porous barriers capture the statistics of sub-grid scale topography and represent the modulation of transport and evolution as a function of depth or elevation. We will use these two concepts to construct an objective algorithm for interpolation of high resolution topography onto coarse grids. The resulting coarse resolution model topography will be shown to accurately represent the key features, both sub-grid scale and resolved, pertinent to the dynamics of an ocean circulation model.

2. Representation of topography in models

Fig. 1a depicts a widely used low-order representation of topography in z-coordinate² ocean models. The topography is considered impermeable and is implemented by adjusting the vertical extent of ocean model control volumes (grid cells) to match the topography and imposing no mass flux (flow) both through the rigid bottom and the exposed side walls of the topographic columns. Adcroft et al. (1997) referred to this representation as partial-step topogra-

phy to distinguish it from the traditional practice of adjusting the topography to match the model vertical grid (“full step” topography). The topography is piecewise constant in the horizontal and thus of limited accuracy. Some improvement in accuracy can be achieved by allowing piecewise variation of topography within the cell (or between), as depicted in Fig. 1b, referred to as shaved cells (Adcroft et al., 1997). Both the partial step and shaved cell representations of topography are implementations of the cut-cell method where a regular grid is cut by a solid body (Berger and LeVeque, 1989; Ingram et al., 2003). The cut-cell method has proven beneficial in high-resolution z-coordinate atmospheric models (Steppeler et al., 2002; Yamazaki and Satomura, 2010; Lock et al., 2012). Layered models (stacked shallow water, isopycnal, and other Lagrangian general-coordinate models) tend to use non-linear transport methods (e.g. the piecewise-parabolic method, PPM, Colella and Woodward (1984)) for mass or thickness which implies a reconstruction of topography. We consider such implicit representations of topography to be in a similar class of representation as shaved cells but of potentially higher order (due to the transport scheme). However, the data used for the reconstruction of topography is the same cell-mean topographic data used for the step representations.

In Eulerian coordinate models, the cut cells method results in a set of face areas and a volume for each cell, as illustrated in two-dimensions in Fig. 2. A given shape of topography unambiguously determines the areas and volumes but the reverse is not true: a given set of areas and volumes can be interpreted as derived from an infinite set of topographic shapes with short scale variations (Fig. 2a). Concave topography within the cell tends to increase the volume and leads to more capacity or inertia for the cell: the concave cell has more mass and so a given mass flux will lead to a reduced tendency relative to a convex cell with the same areas and mass flux. Contrarily, a convex cell has a reduced capacity and thus becomes more sensitive to an incremental flux. This effect leads to the “small cell” conditional numerical stability that has been addressed in several ways. Adcroft et al. (1997) simply adjusted the topography (which changes both the areas and the volume) to avoid cells smaller than a nominal value. Steppeler et al. (2002) left the areas unchanged but artificially expanded the volumes to obtain the most stability. This method was called “thin walls” because by expanding the volume to the notionally full value but leaving the areas untouched, the geometry looks like a collection of infinitesimally thin walls. While they used this concept to stabilize the model, we consider applying the concept as a representation of topography that is actually narrow compared to the grid-scale, as described next.

2.1. Thin walls

If the peaks (ridges) in the real topography happen to line up with the model grid, the cut cell method naturally captures the blocking effect of those ridges (Fig. 2b). Fluid cannot laterally flow between cells below the elevation of that ridge. This is true even for very narrow ridges, with scales that could otherwise not be resolved. This is not to say that the model can resolve the associated (sub-grid scale) dynamics, but it can resolve the geometrical effect of the blocking. In the extreme limit, the geometrical consequences of an infinitesimally wide, knife-edge ridge can be represented with the finite-volume method if the ridge lines up with the model grid cell edges.

Conversely, if the peaks (ridges) of the real topography occur in the cell interior, the blocking effect is lost in the discrete representation (Fig. 2c), unless some alteration is made. In the scenario shown, fluid can laterally flow into and across the cell at elevations below the unresolved ridge (thin horizontal dotted line). The reduction in volume of the cell (due to the convexity) does not represent the blocking effect. In order to retain the blocking effect,

¹ Most gridded data products document the datum properly and in some data sets, the value is the median elevation of observations in the cell, not the mean.

² We use the term z-coordinate loosely to include most vertically Eulerian models, namely those using geo-potential, z^* , pressure, p^* coordinates and the many variants thereof.

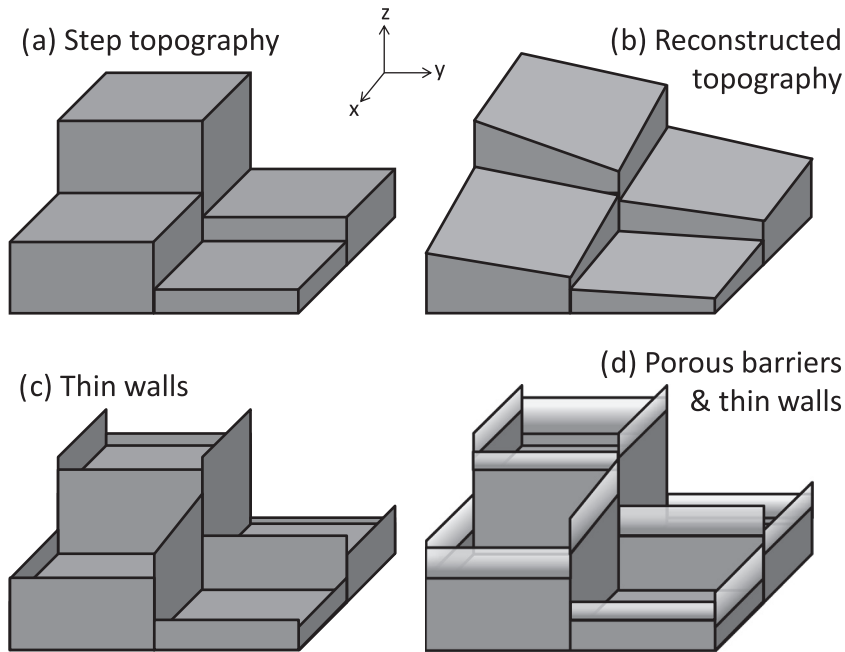


Fig. 1. A schematic perspective view of four ways of representing topography at a given resolution. Each depiction shows how the topography is represented in four model grid columns. (a) Step topography is the most widely used representation in z-coordinate models. (b) Reconstructed topography allows for smoother variation either within or between cells. (c) Thin walls allows the effective topography at cell edges to be taller than the bottom of adjacent cells. (d) Porous barriers extend thin walls by modulating the effective width as a function of elevation.

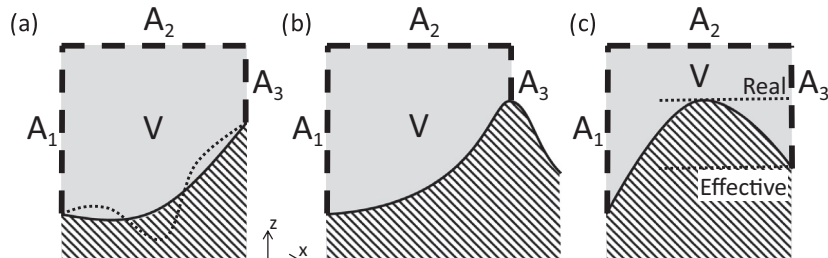


Fig. 2. Two dimensional schematics of the cut-cell method. In each panel, the actual topography is indicated by the striped region and from it the shaded cell volume, V , and face areas, A_i , (thick dashed lines) can be calculated. (a) A second topography indicated by a dotted line yields the same areas and volume, illustrating the non-unique determination of topography. (b) If topographic peaks line up with the cell edges, then the resulting areas accurately reflect the blocking effect of topography. (c) If the topographic peaks appear in the cell interior, the blocking effect of the peak is lost, even though the inertia (capacity) of the cell is correctly reduced. Fluid can flow into and across the cell at a lower elevation than the real peak elevation should permit (dotted line).

either the grid edge must be moved (the unstructured grid paradigm) or at least one of the face areas must be adjusted. Adjustment of a face area is effectively moving the position of the interior ridge, much as coastlines have been snapped to model grids in many traditional fixed horizontal-grid models.

Here on, we will refer to knife-edge ridges aligned with cell edges as impermeable thin walls and we will make use of thin walls to describe connectivity between columns later. We will also extensively use the process of moving interior ridges to cell edges when considering how to objectively interpolate topography while retaining some appropriately approximate connectivity.

Partial step and shaved cell representations of topography are designed to represent resolvable variations in topography. The thin walls representation (Fig. 1c) specifically permits unresolvable (narrow relative to the horizontal grid spacing) topographic features in the form of knife-edge ridges. Such ridges can inhibit transport from one cell to another below some depth, even if the cells in question are generally deeper than the ridge.

A thin wall representation of topography, exactly as we define here, was used in the Hamburg Large Scale Geostrophic (LSG)

Ocean Circulation Model (see Fig. 2 of Maier-Reimer and Mikolajewicz (1992)). There, the topography is defined as residing on Arakawa E-grid vector points and the cell-center depth is normally the deepest of the edge values. Despite the potential for representing narrow barriers, it appears that their method has not been adopted by any other circulation model since LSG.

In principle, a model that can use the cut-cell method can fairly easily adopt thin walls. For instance, the MITGCM (Marshall et al., 1997) uses three-dimensional arrays to store the face areas and volumes of each grid cell with no hard restrictions on how they are set. Appropriate initialization of these areas and volumes can implement any of the partial step, shaved cell or thin wall representations of topography.

2.2. Porous barriers

Thin walls are natural for describing non-connectivity i.e. the condition that below a certain depth, fluid on either side of the thin wall should not be able to communicate. Finding and defining such a deepest connectivity depth is relatively straight forward, as will

be described later in Section 3. Topography, however, is multi-scale and, inconveniently, does not occur in piecewise constant sections. Instead, a profile of depth along a model cell grid edge contains a spectrum of features bounded from below by the minimum connectivity and from above by some peak height, as illustrated in Fig. 3a. A conventional model wishing to represent some gross measure of this profile can use only a single value for the depth on the edge (even if using thin walls which might use the minimum connectivity depth, for example). The challenge here is that the “best” value depends on the perspective and aims of the application. For instance, for barotropic dynamics or depth integrated tracer budgets, one might expect that the best value should be the mean depth. However, for over-flows, the minimum depth is a more relevant depth to choose since the sill depth of an overflow helps determine the water-mass properties.

The porous barriers representation we propose here, provides a distribution of effective width on an edge, as a function of height above the minimum depth of connectivity. The effective fractional width (of connectivity) is zero below the deepest connectivity depth, is one above the tallest feature, and can vary in some monotonic fashion between these two depths (Fig. 3c). The consequence is that inter-column transport is geometrically modulated as a function of elevation. Fig. 4a illustrates this modulation on the edge of a column. Fluid below the lower surface (R) cannot pass between the two columns shown, assuming R is at or below the minimum topography. Fluid above the upper surface (G) is unimpeded by topography if G is at or above the tallest topographic features. Although the elevation difference between the three surfaces ($G-B$ and $B-R$) is approximately the same, the area, A_{RB} , available for lateral transport of fluid in the layer $R-B$ is significantly less than the area, A_{BG} , available to transport fluid in layer $B-G$.

The vertical profile of the effective fractional width is equivalent to the cumulative pdf (probability distribution function) of depth on the edge (Fig. 3c), which can be found simply by sorting the high-resolution point-wise depths along the edge. The shape of the distribution may be quite convoluted (the pdf is very non-Gaussian, Fig. 3b) but we will later propose using a simple three parameter fit. The concept is independent of the choice of curve-fit.

The individual channels depicted in Fig. 4a, and the implied multiple distinct pathways between columns, cannot be resolved or represented in the coarse model. From the perspective of the coarse scale columns, all that matters is their aggregate effect of

providing increasing effective width for transport with higher elevation. Transport between the coarse scale columns can not distinguish between this aggregated representation of the fine-scale multiple-channel topography and a single channel with the shape of the fine-scale pdf.

The structure depicted in Fig. 4a should not be interpreted as providing lateral (along edge) information with which gradients and dynamics can be calculated. Instead, the information is of a bulk nature and for this reason we schematically depict the porous barriers as a fuzzy region above the impermeable thin walls in Fig. 1d.

The above discussion describes the modulating effect of a porous barrier on lateral transport or fluxes. A similar “porous media” effect applies to the capacity or inertia of a grid cell. Fig. 4b depicts a single column with a porous media representation of sub-grid scale topography in the interior of the column. As discussed earlier, topographic blocking of flow by interior ridges cannot be represented by a single (or multiple) volume parameter. However, the geometrical effect on capacity/inertia of the column can be captured: there is less volume below the lower surface (R) than between the other surfaces, so a given volume flux divergence below R will lead to a more rapid change in elevation of R than for the other surfaces. It is not possible to faithfully represent sub-grid cell ridges that separate the cell into multiple bodies of fluid since the blocking effect is lost, even though the displacement of fluid can be captured. Open area for transport between columns in and out of a layer in Fig. 4b is strictly determined by the intersection of the layer surfaces with the topography on the edges of the cell, not the interior (depicted in Fig. 4a).

2.3. Describing porous barriers and volumes to a model

In an Eulerian frame, a conservation law for scalar ϕ takes the form

$$\partial_t \phi + \nabla \cdot \mathbf{F} = 0, \quad (1)$$

where \mathbf{F} is the flux of ϕ and $\nabla \cdot$ is the three-dimensional divergence operator. The finite volume method integrates the conservation law over a finite volume, \mathcal{V} to yield

$$\partial_t (\mathcal{V}\phi) + \delta_i(\mathcal{A}_x F_x) + \delta_j(\mathcal{A}_y F_y) + \delta_k(\mathcal{A}_z F_z) = 0, \quad (2)$$

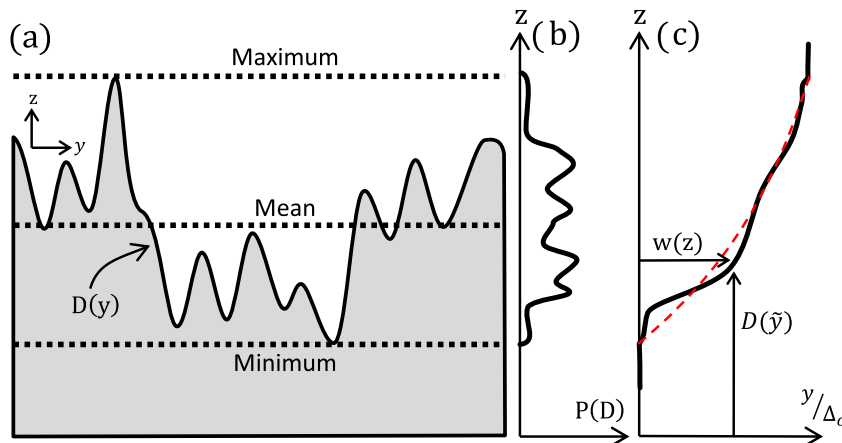


Fig. 3. (a) A schematic profile of unresolved topography, $D(y)$, along a single model grid cell edge (also shown in Fig. 4a). The deepest (minimum) topography is the level below which fluid is entirely blocked, the maximum is the level above which fluid is completely unimpeded by topography. Often the mean topography is used in models but this can under-estimate deep connectivity. (b) The pdf of topography, $P(D)$, is bounded (zero above/below the maximum/minimum) and is very non-Gaussian. (c) The effective fractional width, $w(z)$, at an elevation z , is equivalent to the cumulative pdf of depths, which can be found by sorting the depth profile, $D(\hat{y})$. We suggest a simple curve fit (red dashed curve) to represent the cumulative pdf (see text and A). (For interpretation of the references to color in this figure legend, the reader is referred to the web version of this article.)

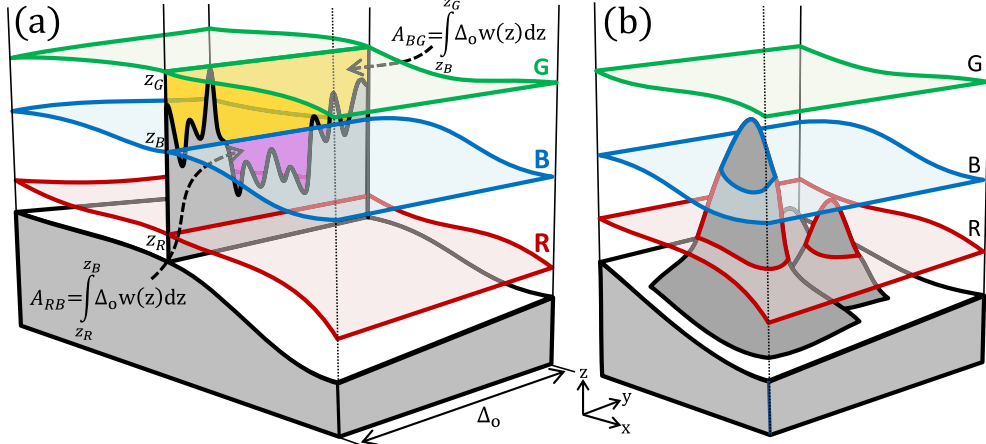


Fig. 4. (a) A perspective schematic of an edge wall with sub-grid scale topography modulating transport across the edge between columns. When the lower surface (R) is at or below the deepest topography, fluid below R is completely blocked. Similarly, when the upper surface (G) is at or above highest topography, transport above G is unimpeded by topography. Fluid between the lower (R) and middle (B) surfaces can flow through the reduced open area, A_{RB} (magenta). Fluid between the middle (B) and upper (G) surface has a larger area, A_{BG} (orange), available for transport than A_{RB} . The location and existence of individual valleys/peaks is lost in the formulation; only their aggregate effect is retained via an effective open width, $w(z)$ (depicted in Fig. 3c). (b) A perspective schematic of how the volume of fluid in a cell can be modulated with elevation; deeper in the water column there is less lateral area available to contain fluid. Interior ridges, that separate the fluid regions cannot be represented. Transport in/out of a layer within the cell is determined only by the intersection of the layer with topography on the edges (as shown in panel a).

where ϕ is now the mean value for the volume, the sub-scripts indicate directions and the δ_{ijk} notation indicates a simple difference of normal fluxes across the volume. The volume, \mathcal{V} , and areas, $\mathcal{A}_{x,y,z}$, need not be constant in time and indeed in most ocean circulation models some time dependence is assumed.

We denote the range of topography on a cell edge or volume by the minimum value, $z = D_-$, and the maximum value, $z = D_+$ (elevation z is positive upwards). The cumulative pdf of topography on that edge, $f(x)$, is linearly related to the sorted topography, $D(x) = D_- + (D_+ - D_-)f(x)$. If we know, or have a good model of, $f(x)$, then we can construct an equivalent pdf description of the fractional width of fluid as a function of elevation, $w(z)$ (details of this equivalence are given in A). On a column edge, if we denote the nominal element length by Δ_o , the open width at some depth z is $\Delta(z) = \Delta_o w(z)$, and the area of fluid between some depth z and the topography is then given by

$$\mathcal{A}(z) = \int_{-\infty}^z \Delta(z') dz' = \Delta_o \int_{D_-}^z w(z') dz'. \quad (3)$$

The area of a control volume side-face (\mathcal{A}_x or \mathcal{A}_y in Eq. 2) is the difference in $\mathcal{A}(z)$ for the bounding interfaces above and below the volume. Similarly, if the nominal areal footprint of the column is denoted A_o , then the open vertical column area at some depth is $A(z) = A_o w(z)$, now applying $w(z)$ to the column instead of the edges. This provides the values for \mathcal{A}_z at the top and bottom of the cell. The volume of fluid below some depth z is then given by

$$\mathcal{V}(z) = \int_{-\infty}^z A(z') dz' = A_o \int_{D_-}^z w(z') dz'. \quad (4)$$

There are many ways to construct $f(x)$ (or $w(z)$). Appendix A details a three parameter curve fit but a higher order model or even the raw pdf could be used. However, for the purposes of the discussion here, we assume that the description of topography will require only three parameters, the minimum, D_- , the maximum, D_+ and the mean, \bar{D} , and that those parameters will be available for both columns (cell centres) and grid edges (cell faces).

3. Objective regridding of high-resolution topography

The regridding algorithm works by recursively coarsening four fine cells at a time into a single coarse cell. Data is stored for both

the cell centres (columns) and the cell edges. This provides three times the degrees of freedom than would be obtained by just storing data for cell centres. Moreover, we carry forward three parameters for each center or edge (minimum, maximum and mean) which yields a net factor of nine times the degrees of freedom compared to a more standard representation of topography. The source code has been made available in the public domain (Adcroft, 2013).

3.1. Fine grid generation and interpolation

To arrive at the intended target grid via repeated coarsening, the source data must first be provided on the finest grid that is a power of 2 finer than the target. To find the finest grid, we repeatedly refine the target grid by factors of 2 until every cell on that fine grid is locally smaller than any cell of the source data in its vicinity. Source topography is interpolated to the finest grid using nearest neighbor rules (i.e. a first order accurate interpolation). This process ensures that no extreme data values (local valleys or peaks) are lost or generated. The geographic position and horizontal breadth might be shifted by up to half of the width of the fine cell. We use this low-order interpolation to preserve connectivity of the source data, but it is only used in the initial interpolation to the finest grid.

3.2. Initial thin wall parameters

Starting on the finest grid, the interpolated topography has only cell mean values. The initial data is interpreted as piecewise flat, again to preserve connectivity, so that the minimum, mean and maximum of cell and edges are all the same. Thin wall values are generated to be consistent with this step topography interpretation. Thereafter, connectivity is always determined in terms of the edge values.

3.3. Relationship between levels of refinement

At each level of recursion, the only data available are the cell and edge values on the immediately finer grid of twice the resolution; information does not skip across levels of recursion. We carry forward an effective minimum, an effective average and effective maximum. The true minimum, average and maximum are also carried forward as a trivially calculated diagnostic but play no role in

the algorithm. We use the true values solely for comparison in analysis.

3.4. Diagnose coarse connectivity

At each level of refinement, the first step is to diagnose six “connectivity” parameters for each coarse cell. Connectivity is defined in terms of the “effective minimum” wall values. Each connectivity parameter is the value of deepest connection across the coarse cell from one side to another, in one of six directions, two directly across (north-south and east-west) and four across each corner (south-to-west, west-to-north, north-to-east and east-to-south). For each of the north-south and east-west directions, there are eight possible paths on the fine grid that could connect the coarse cell to the south to the coarse cell to the north, as illustrated in Fig. 5 for the north-south direction. Along each possible path, the tallest thin wall value determines the depth of the path, and the deepest of all eight is assigned as the north-south connectivity depth. The east-west direction is handled similarly. For each of the four diagonal directions, there are seven possible paths connecting the coarse cell to the south to the coarse cell to the west, as shown in Fig. 6 for the south-to-west direction. Each of the other three corner connections are diagnosed similarly. These six con-

nnectivity parameters are subsequently used as constraints to test whether a deeper pathway is artificially introduced during the coarsening of topographic data.

3.5. Removing tall corners

Within each coarse grid cell, the four fine grid cells might represent up to four separate bodies of fluid. Before coarsening the topographic data from fine to coarse grid, adjustments are made to the fine grid, re-arranging the internal thin walls to represent something closer to only one body of fluid. The first re-arrangement identifies tall corners (Fig. 7a) in which the two tallest interior thin walls (blue lines) forming corners are pushed out as follows. The lower value of the two inner walls (blue lines) is chosen as a potential new value for the outer walls (red lines). For each of these outer lines the value is replaced if the outer wall would be raised. Both of the inner tall ridge values (blue) are then assigned the taller of the remaining (as yet) unused inner walls. At the end of this adjustment, cells that underwent this adjustment will have three of the four inner walls with the same value. Cells that did not undergo adjustment must have the two tallest center edges aligned in a straight ridge, dealt with next.

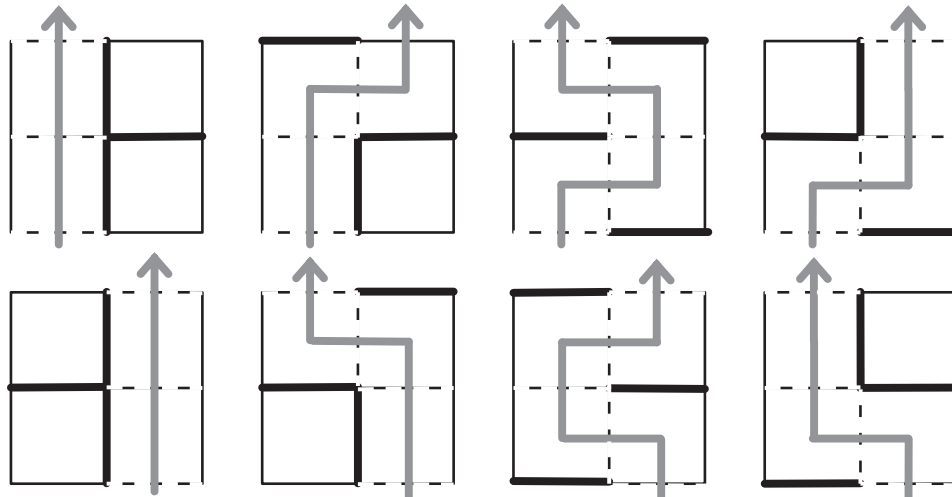


Fig. 5. The eight possible pathways of deepest north-south connectivity (grey arrows) across a coarse grid cell (comprised of four fine grid cells). The dashed lines indicate deep thin walls that are all deeper than the taller (thick lines) thin walls. Each deepest pathway is uniquely defined by the deepest (dashed) walls whereas some pathways can have multiple tall (thick) wall configurations which do not alter the deepest connectivity.

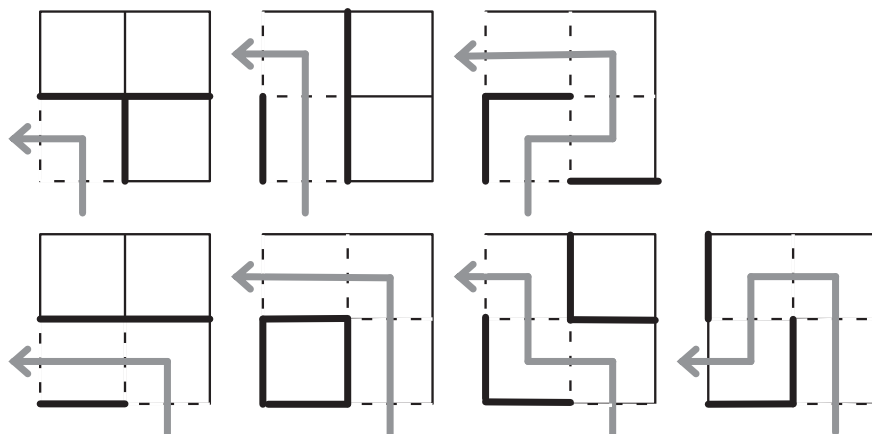


Fig. 6. As for Fig. 5 but for the seven possible pathways of deepest south-west diagonal connectivity across a coarse grid cell.

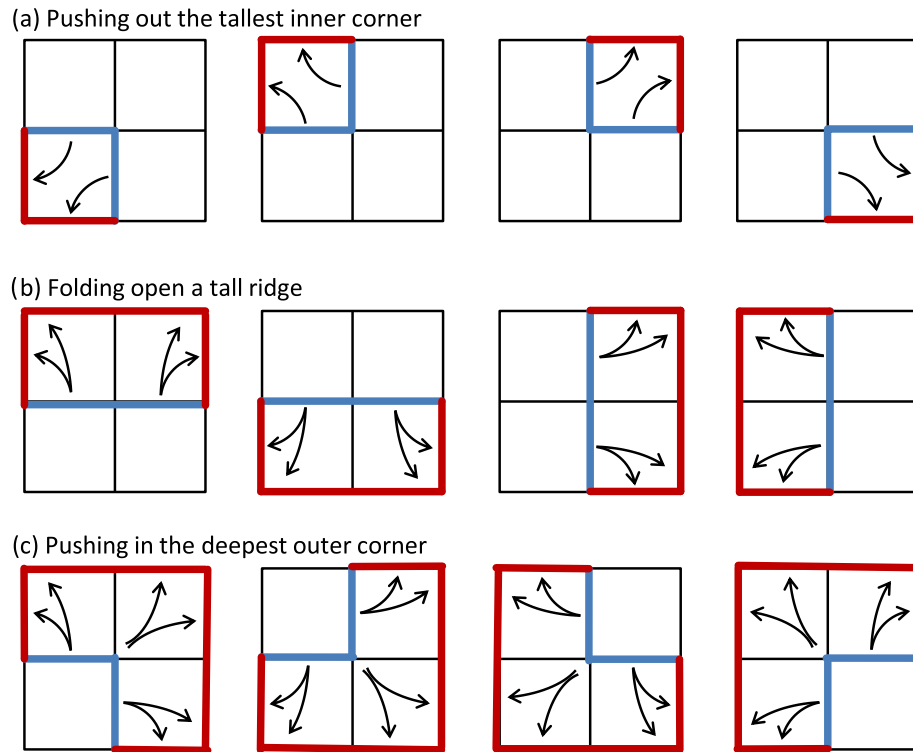


Fig. 7. Internal fine grid wall adjustments. (a) If the two tallest thin walls form a corner (four blue scenarios), they are pushed out (blue) thereby removing that body of fluid that was disconnected from the rest of the cell. (b) If the two tallest thin walls form a straight ridge, they are folded open in the direction of tallest thin walls on either side. (c) The two inner walls associated with the deepest corners are pushed into to create a single depth cell. (For interpretation of the references to colour in this figure legend, the reader is referred to the web version of this article.)

3.6. Removing interior ridges

The second re-arrangement identifies straight ridges defined where the lower of a straight pair is equal³ to or higher than the highest of the opposing pair (Fig. 7b). The lowest value on the taller ridge (blue) is considered the potential new value for the outer walls. The four outer walls on the opposite side from the deepest inner ridge are then assigned the potential value when it would raise that wall. The three tallest inner walls are assigned the deepest inner wall value. At the end of this adjustment all the inner walls have the same value. Again not all of the cells meet the criteria for adjustment but any that underwent the previous “corner push” adjustment do meet the criteria for the “ridge folding”.

3.7. Expansion of deepest corner

The only cell that will not have had interior wall adjustments are those with all equal wall values. This typically only happens for very flat topography which essentially means that the column as a whole is a large barrier. After the two fine grid adjustments described, all the inner edge values are equal but there may still be multiple bodies of water represented because the eight outer edges may be deeper than the four inner edges. The third fine grid adjustment selects the corner with the deepest corner transport defined as the higher of the two outer edges on a corner. The deeper of the associated inner edges is considered the potential new value for the six outer edges opposite from the deepest corner and the value used if it would raise that edge element. The inner edges are all assigned the same value. The result of this operation is a hollow C-shape with inner edges all of the same value.

The net result of each of the three fine grid adjustments above is that the edge values are ordered in some sense so that there are no interior barriers within the coarse cell. The four fine cells considered together are effectively representing a single body and thus a coarse cell can now more reasonably approximate the connectivity of the four fine cells.

3.8. Coarsening

Thus, after adjusting the fine grid edges, we can now coarsen the data as follows. The minimum and maximum coarse edge values are assigned the minimum/maximum of the two associated fine grid edge values. The mean edge value is calculated as a two-dimensional spatial average of the four abutting cell averages. The coarse center values use all four fine center values.

3.9. Applying coarse grid constraints

The coarse grid connectivity is compared with the six connectivity parameters calculated before any fine grid adjustments were made (Figs. 5 and 6). There are four degrees of freedom (minimum value on each coarse edge) that are constrained by six deepest pathways. There is no way to ensure that the coarse diagonal and cross cell pathways equal the diagnosed fine grid pathways. For the most part, the coarse pathways will not be deeper than the fine-grid pathways but for the infrequent exceptions we make a final adjustment to the coarse edge values to ensure no new deepest pathway is created. Each pathway (North–South, East–West, South–West, South–East, North–West and North–East) is compared independently and if the coarse pathway is too deep the higher of the two coarse edges involved is raised to make the pathway equal to the fine-grid pathway. This adjustment applies only to the minimum values and any mean and maximum edge

³ The definition includes the equality of heights in order to capture “T”-shaped ridges which would otherwise need to be considered separately.

values that are inconsistently ordered are bounded so that the minimum, mean and maximum values are correctly ordered.

3.10. Bounding statistical values

Finally, the value of the effective mean is bounded to be above the effective minimum value and similarly the maximum value is bounded to be above the mean. This is needed since we have been moving the effective minimum around on the fine grid to approximately retain connectivity but not moving the other moments around with it.

Overall, the adjustments we described are arbitrary but they were chosen to bias towards retaining deeper connections without opening new connectivity. The first “corner pushing” favors the larger aerial fraction of the cell, while the “ridge folding” and second “corner pushing” favor deeper connections.

4. Illustrative examples

To illustrate the qualitative advantage of the thin-wall representation and interpolation algorithm over more conventional approaches, such as partial-steps and spatial averaging, we consider several regions of oceanographic importance. Fig. 8 shows the two regions of the Indonesian through-flow and the Denmark Strait-Iceland-Faroe bank, plotting the raw 1' data (version 14.1) from Smith and Sandwell (1997). Both these regions have topographically constrained overflows and are of global oceanographic importance. Indicated in Fig. 8a is the Lombok strait which allows water to spill from the Java Sea into the Indian Ocean across the otherwise effective barrier of the southern Indonesian islands. The Ombai and Timor channels are deeper and allow deeper water from the Banda Sea to reach the Indian Ocean. The Denmark Strait (Fig. 8b) provides the deep pathway for Denmark Strait Overflow Water to spill into the North Atlantic via a relatively broad, but diagonal, channel (on this grid orientation) while Iceland-Scotland Overflow Water spilling through the Faroe bank channel has to take a more circuitous route.

Fig. 9 shows the region of the Indonesian through-flow at three representative resolutions; $\frac{1}{4}^\circ$, $\frac{1}{2}^\circ$ and 1° . The topography shown in the left column is calculated using a conventional spatial average of high-resolution topographic data and is the depth that a partial-step ocean model would be assigned at each resolution. Note the barrier formed by the southern Indonesian islands (at about $8\frac{1}{2}^\circ S$) begins to disappear even at $\frac{1}{2}^\circ$ resolution and is completely

absent on the 1° grid. The Timor ($11^\circ S$, $123^\circ E$) and Ombai ($9^\circ S$, $125^\circ E$) channels become shallower with coarser resolution. In contrast, the right column shows the minimum depth of connectivity calculated using the thin wall algorithm. The connectivity is defined by the edge values which are drawn as colored lines. Here, at each resolution, the island-made barriers are retained, often collapsing to a thin wall, and the deep channels are still apparent and, for the most part, contiguously connected. Aesthetically speaking, the thin-wall depiction is more representative of the original high-resolution data (Fig. 8a) than the spatially-averaged depiction (left column). Other methods, such as sub-sampling or different statistical downscaling, might fair better but the reduction of resolution using only a single parameter at a cell center inevitably will not be able to depict the complexity of topography as well as the thin-walls which has at least three times the data content due to the data residing on the cell edges.

The mean and maximum values produced by the thin wall algorithm are shown in Fig. 10. These are, for the most part, the simple areal average/maximum except where the connectivity adjustments raised the minimum above the mean/maximum, in which case the mean and maximum are bounded from below. While a plot of the minimum value renders a recognizable depiction of the real world, the plots of the mean and maximum values need more care to interpret. The mean is at least higher than the minimum values but in some cases can be positive (above sea level) even though the edge or cell may contain ocean. The positive value does not imply that oceanic transport is necessarily blocked since “blocking” is solely determined by the value of the minimum parameter for an edge. In the instances where the mean is above sea-level and the minimum is below sea-level, it means that only a partial section of the edge is open for transport. We have found it particularly difficult to visualize all three parameters (minimum, mean and maximum) simultaneously for both edges and cells in a satisfactory way.

A similar comparison of spatial-averaging and the thin-walls algorithm is shown for the Denmark Strait-Iceland-Faroe bank region in Fig. 11. Here the disappearance of the Faroe Islands on the 1° grid in both depictions could be argued to be acceptable since they do not present a barrier to flow in any direction for a 1° wide cell. The mid-Atlantic ridge, south-west of Iceland, depicted by averaging gradually becomes smoother and deeper with coarsening resolution so that it is barely visible as a barrier at 1° . In contrast, the thin-wall approach retains the tall peaks and the mid-Atlantic ridge is identifiable as a contiguous but zigzag, ridge; the

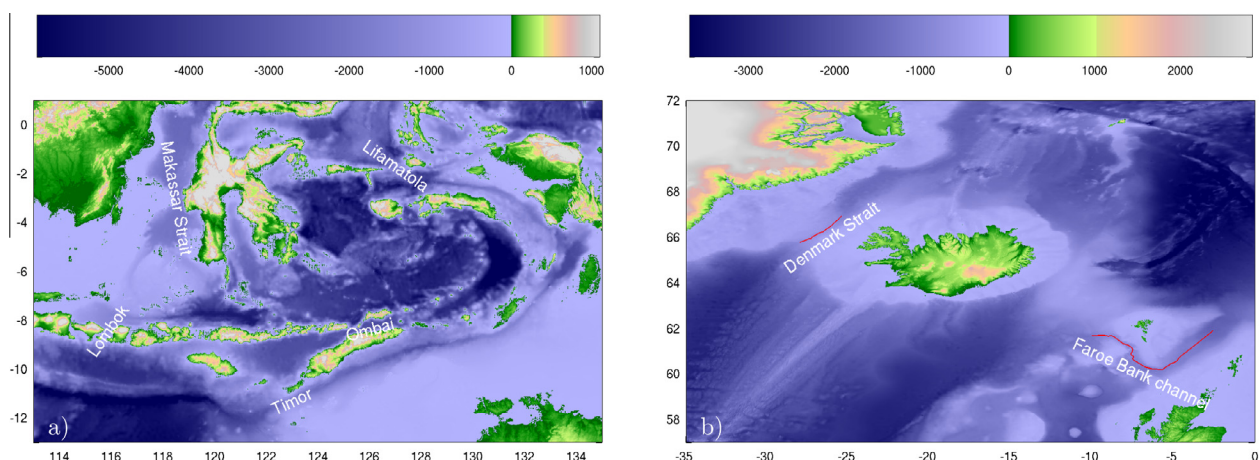


Fig. 8. Topography of (a) Indonesian through flow region and (b) Denmark strait-Iceland-Faroe channel region from Smith and Sandwell (1997) at 1' resolution. Note the different color scales for the different regions. In all geographic plots, the topography is positive up (zero is mean sea-level) given in units of meters, the x-ordinate is longitude ($^{\circ}$ E) and y-ordinate is latitude ($^{\circ}$ N).

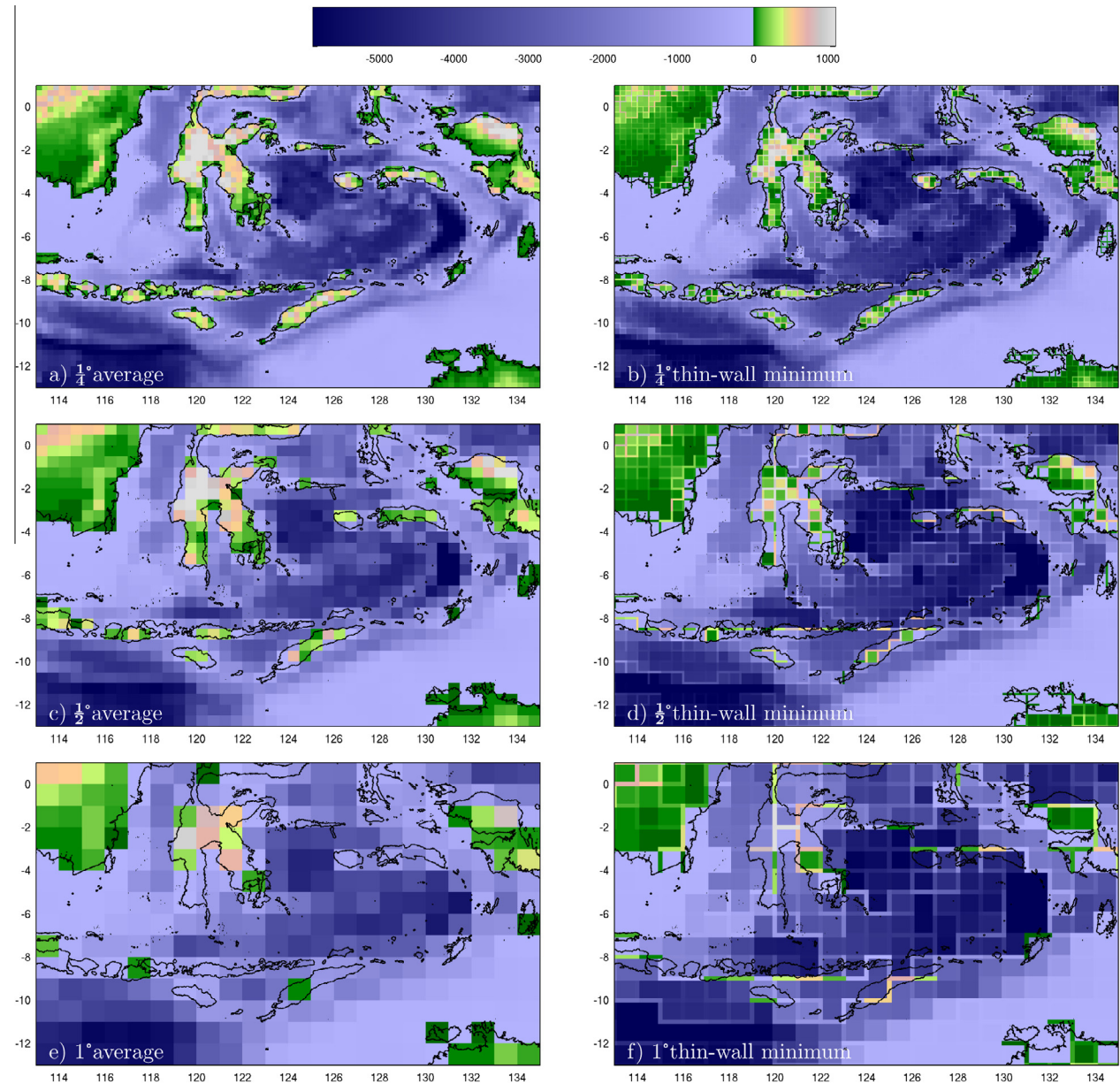


Fig. 9. Topography of Indonesian Through Flow region at three resolutions ($\frac{1}{4}^\circ$ – top, $\frac{1}{2}^\circ$ – middle, 1° – bottom) and using either the traditional spatial-averaging method (left column) or the thin walls algorithm (right column, showing only the deepest values). Note that the cell-center minimum is always at least as deep as the deepest edge value as a result of the thin-wall regridding algorithm (Section 3).

zigzag arises because the ridge is diagonal in orientation. The Denmark strait retains deeper values at the sill (numerical values will be provided in the next section) and the Faroe bank channel is also still identifiable and contiguous, even at 1° resolution and despite the circuitous path.

5. Evaluation of connectivity: sill depths

In the two examples of Section 4, the visualization of the deepest connectivity (thin-wall minimum value) clearly indicates that thin-walls provide a more faithful structural representation of the original high-resolution data. We now examine how well the method performs numerically.

Fig. 12 shows the sill depths for four oceanographically important Straits: Denmark Strait, the Faroe Bank Channel, the Strait of Gibraltar and Bab-el-Mandeb (Red Sea overflow). We considered

four different gridded data products. ETOPO2v2 is a $2'$ blended product (NGDC, 2006) and the oldest considered here. Smith and Sandwell (1997) is a nominally $1'$ dataset limited to latitudes between 80°S and 80°N . ETOPO1 is a $1'$ product (Amante and Eakins, 2009) which blends various other products including the Smith and Sandwell product. Gebco 08 version 20100927 (GEBCO, 2010) is the highest resolution product considered which is a blended $1/2'$ data set. In this analysis, we diagnose the sill depth defined to be the deepest depth that water can flow from one basin into another as found by a flooding algorithm. For each of the four sills, we show the diagnosed sill depth (cross marks) at the corresponding resolution of the gridded data. Note that the various gridded products do not agree on these sill depths. For instance, the Bab-el-Mandeb sill is 137 m, 113 m, 126 m and 103 m deep in GEBCO, Sandwell, ETOPO1 and ETOPO2v2 respectively. There are few references to the actual sill depth; paleo-sea-level studies typically cite 137 m depth from Werner and Lange (1975) while some

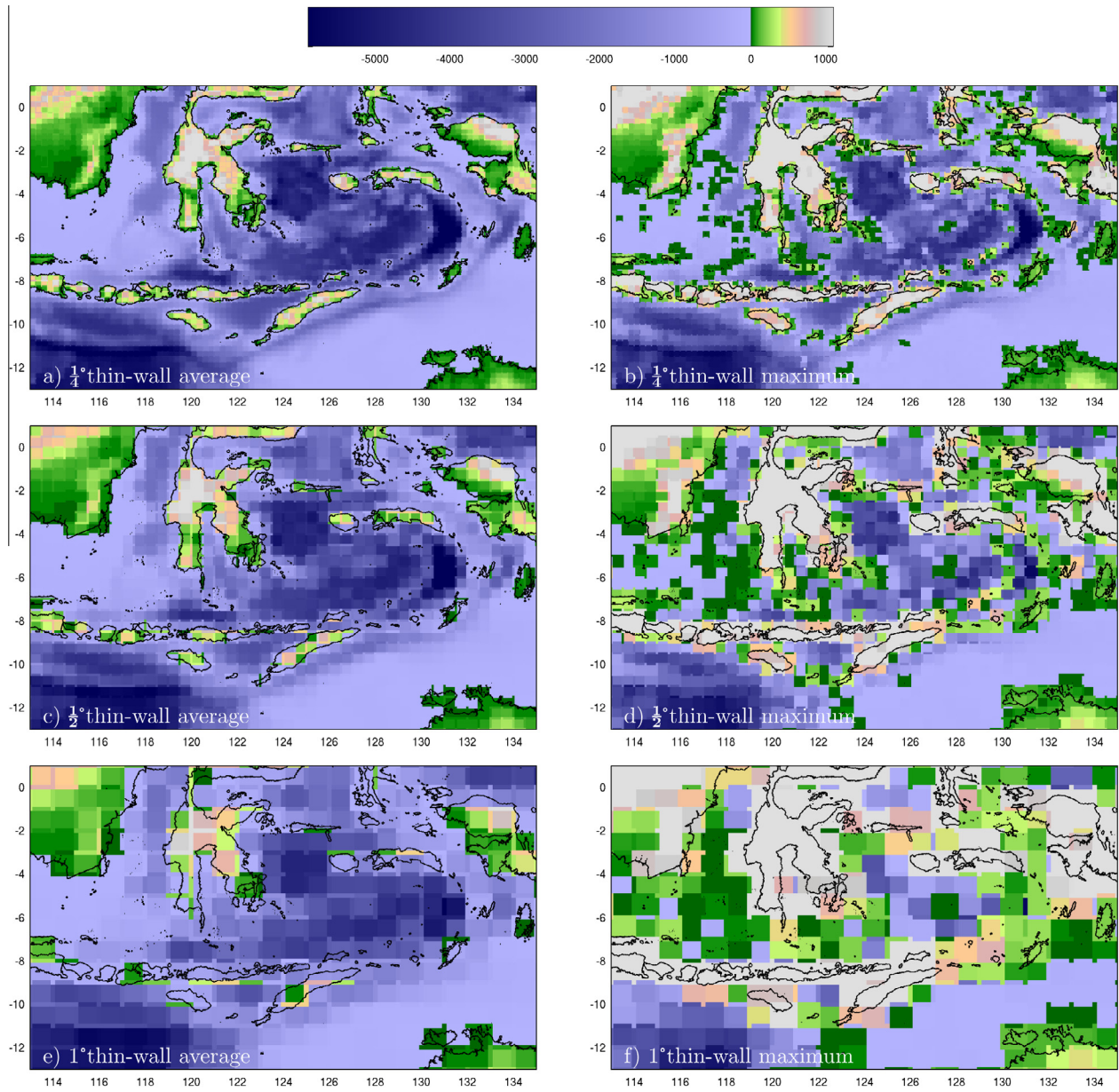


Fig. 10. As for Fig. 9 showing the thin-wall mean (left) and highest (right) values. Note that a positive (above sea-level) mean or maximum value does not imply that the thin-wall is necessarily closed to oceanic transport, an aspect which is determined by the deepest value (shown in right column of Fig. 9). The cell-center mean values (left) match those shown in the left column of Fig. 9 except where connectivity required alterations (the mean cannot be below the minimum). The map of maximum values is less recognizable and indicates the depths below which modulation of fluxes/inertia begins.

physical oceanographic literature site 163 m depth (Pratt et al., 1999). Highlighting such discrepancies serves to make two points: i) the gridded products should not be considered definitive and ii) the actual bathymetry is often not known.

For each of the gridded products, we generate an ocean model topography using spatial averaging for several resolutions ranging from $1/10^\circ$ - 1° (square marks, colored according to original gridded product). Generally, the coarsest model sill depth is always shallower than it should be presumably due to the typical saddle shape of topography at sills. However, the error is not monotonic nor predictable as a function of resolution. For the two shallow sills shown, the sill becomes completely land blocked.

In contrast, the objective regridding algorithm (Section 3) is able to retain the exact original sill depth, using the minimum edge depths, at all resolutions for three of the four sills shown. The thin-

wall Bab-el-Mandeb (Red Sea overflow) sill depth does vary with resolution but only by 13 m which is less than the range of differences between the original gridded products.

We conclude from these results that the thin wall interpolation algorithm is robust and reliable.

6. Impact of porous barriers on dynamics: Tsunami travel time

The sill depth analysis, presented above, focused on the deepest connectivity (minimum elevation) while here we turn our attention to the value of the mean elevation at the edges. The particular distribution of topography between the minimum and maximum is likely to matter most for flow structures contained below or near the maximum topography. The barotropic mode, however, is most dependent on the mean topography because, by definition, the

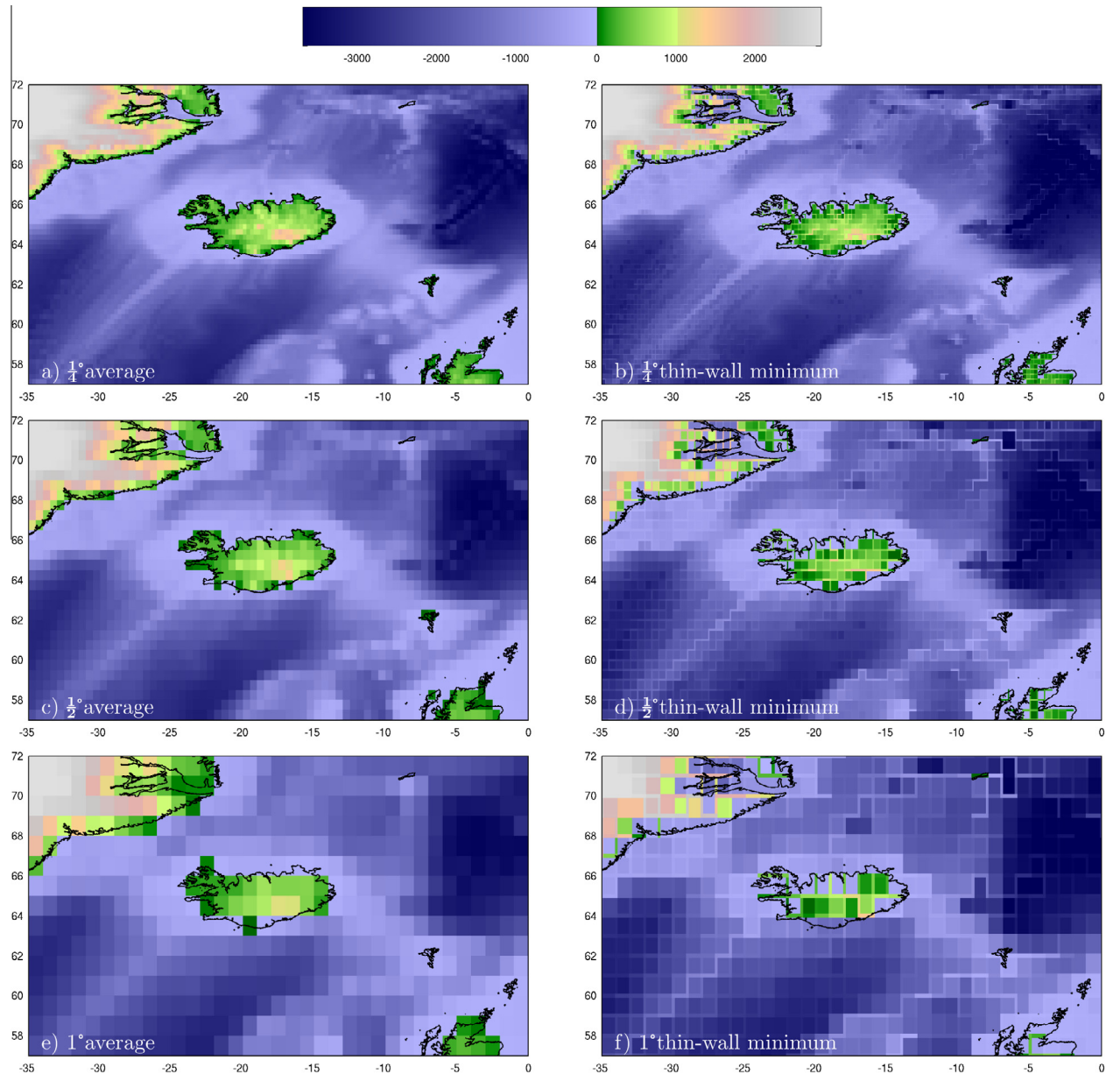


Fig. 11. As for Fig. 9 but for topography of Denmark Strait, Iceland and Faroe Bank Channel. Notice that the Faroe-Bank overflow channel is visibly shallow, south-west of the Faroes, in the 1° resolution, averaging data while the thin-wall algorithm retains the high-resolution channel depth.

mode is integrated over the full depth of the fluid. Thus, barotropic dynamics provide a good measure of the representation of the mean topography. Here, we consider cross-basin travel times for barotropic waves, specifically tsunami.

We use a single-layer shallow water model of the great Sumatra-Andaman Tsunami that travelled across the Indian Ocean on 26 December 2004. The model equations are based on those provided in Section 3 of Harig et al. (2008) that include a bottom friction based on Manning's approach. We drop the lateral viscosity term since we found it unnecessary to obtain a solution and because such scale selective terms can change the solution as a function of resolution. The governing equations are:

$$\partial_t \mathbf{v} + \omega \mathbf{k} \times \mathbf{v} + \nabla K + g \nabla \eta + \frac{gn^2 |\mathbf{v}|}{h^{4/3}} = 0, \quad (5)$$

$$\partial_t \eta + \nabla \cdot (h \mathbf{v}) = 0, \quad (6)$$

where \mathbf{v} is the horizontal velocity vector, η is the sea-surface displacement from resting position, $h = \eta - D$ is the column thickness, $z = D(\mathbf{x})$ is the position of the rigid bottom, $\omega = f + \mathbf{k} \cdot \nabla \times \mathbf{v}$ is the absolute vorticity, $K = \frac{1}{2} |\mathbf{v}|^2$ is the kinetic energy density, g is the free-fall acceleration due to gravity, and n is a friction coefficient (we use $n = 0.015$). The model is discretized on an Arakawa C-grid and stepped forward in time using a forward-backward scheme. The absolute vorticity (ω) is upwind biased so that the vorticity equation, formed by taking the curl of Eq. 5, looks like a forward-in-time, first-order upwind biased transport scheme for the scalar ω . The kinetic energy is also upwind biased using the Godunov scheme. Both of these upwind schemes act so that grid-scale oscillations in either K or ω are numerically dissipated rather than dispersed. The momentum equations are treated the same in all runs. The methods are a mixture of quasi-second order and first order schemes but are robust in that they are not susceptible to extreme noise. The time-step is chosen so that the fastest deep water waves

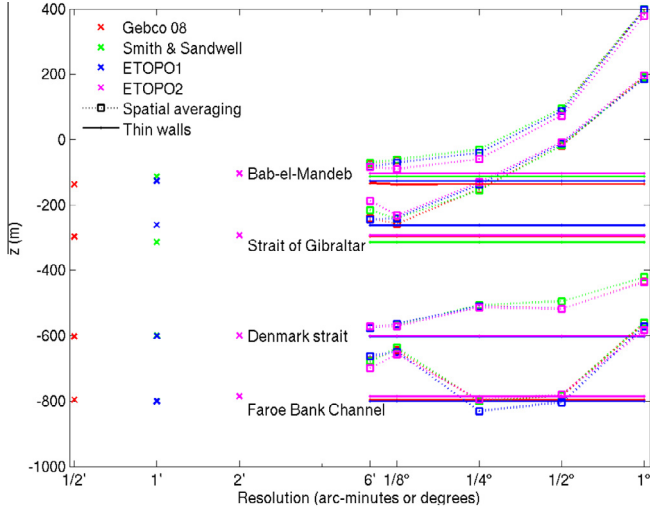


Fig. 12. Illustrative sill depths according to four gridded data sources (Gebco 08, Smith and Sandwell, ETOPO1 and ETOPO2v2) and as represented on derived ocean model grids at various resolutions from each data source. The diagnosed sill depth from the original data is plotted at the resolution of the data (cross marks on the left) and color coded. There are four spatial averaged curves (dotted lines, square symbols) for each sill, color coded to match the data source. The error tendency with resolution is fairly independent of the data source but does differ between sills. There are four thin-wall curves (solid lines with dot markers) for each sill, color coded by data source. For the thin-wall data, three of the four sills have no variation with resolution. Bab-el-Mandeb (Red Sea overflow) does vary but by less than the variation between the original gridded data sets.

are marginally stable and have approximately the same stability parameter for all runs: $\Delta t \sqrt{gH}/\Delta x \approx \frac{1}{2}$.

We consider a range of resolutions from $\frac{1}{2}^{\circ}$ to 1° . The bathymetry is based on the $\frac{1}{2}\text{-min}$ GEBCO_08 gridded data (GEBCO, 2010). The initial conditions are an approximation of those given in Table 1 of Harig et al. (2008) projected onto a 1° resolution grid so that the initial conditions are equivalent for all resolutions considered here (i.e. on the $\frac{1}{4}^{\circ}$ grid, a $1^{\circ} \times 1^{\circ}$ wide block of $4 \times 4 = 16$ cells is displaced at each fault location as if it were on the 1° grid).

Although the topography enters in the friction term, the term that most strongly affects the solution due to the representation of topography is the volume flux in the continuity equation (hu). The various representations of topography we discussed lead to the following discretizations of the zonal component:

$$(hu)_{ppm} = PPM(u_{i+\frac{1}{2}}, \eta - \bar{D}), \quad (7)$$

$$(hu)_{pcm} = PCM(u_{i+\frac{1}{2}}, \eta - \bar{D}), \quad (8)$$

$$(hu)_{step} = PCM(u_{i+\frac{1}{2}}, \eta) - u_{i+\frac{1}{2}} \max(\bar{D}_i, \bar{D}_{i+1}), \quad (9)$$

$$(hu)_{shaved} = PCM(u_{i+\frac{1}{2}}, \eta) - u_{i+\frac{1}{2}} \times \max(\bar{D}_i + \frac{1}{2}s_i, D_{i+1} - \frac{1}{2}s_{i+1}), \quad (10)$$

$$(hu)_{porous} = PCM(u_{i+\frac{1}{2}}, \eta) - u_{i+\frac{1}{2}} D_{i+\frac{1}{2}}, \quad (11)$$

where integer subscripts indicate a cell value, half-integer subscripts indicate an edge value, s_i is the slope of shaved cell topography, the function $PPM(u, h)$ is the flux using the piecewise-parabolic method (Colella and Woodward, 1984) and the function $PCM(u, h)$ is the piecewise-constant method or first-order upstream method, given by

$$PCM(u_{i+\frac{1}{2}}, h) \equiv \max(0, u_{i+\frac{1}{2}})h_i + \min(0, u_{i+\frac{1}{2}})h_{i+1}. \quad (12)$$

See Colella and Woodward (1984) for details of the flux $PPM(u, h)$, but note that PPM is not distributive in h due to the non-linear limiter; i.e.

$$PPM(u, \eta - D) \neq PPM(u, \eta) - PPM(u, D),$$

whereas

$$PCM(u, \eta - D) = PCM(u, \eta) - PCM(u, D).$$

For stability, all fluxes are limited to retain non-negative thickness: $|(hu)| < |PCM(\frac{1}{2} \frac{\Delta x}{\Delta t} \operatorname{sgn}(u), h)|$ even though it is not needed for $(hu)_{ppm}$ and $(hu)_{pcm}$. For schemes (9)–(11), the thickness transport is split into two components, one due to a transport of (dynamic) η and the other due to the static ocean depth, D . In deep water, the dynamic component is small compared to the static component. For this reason we found minimal sensitivity to the use of PPM instead of PCM in schemes (9)–(11) (not shown). The largest sensitivity of results is to the choice of discretization of static topography term, which is the focus of this study. We will label the model results according to the treatment of the static component.

In the porous model, the edge value $D_{i+\frac{1}{2}}$ is the application of Eq. 3 with $z = 0$:

$$D_{i+\frac{1}{2}} = \frac{\mathcal{A}(0)}{\Delta o} = \int_{D_-}^0 w(z) dz \approx \bar{D}_{i+\frac{1}{2}}. \quad (13)$$

The last approximation holds in deep water where the maximum topography does not show above sea-level ($\eta - D_+ > 0$). Since we are interested in deep water waves, we have applied this approximation uniformly, even in shallow regions, to keep the model simple. The Tsunami cross-basin travel times are measured in deep water and so this approximation does not affect the results presented here.

Fig. 13 shows the sea surface displacement after 2 h 20 min from the beginning of the disturbance in two models of different resolutions. Panel (a) is from a $2' (\frac{1}{30}^{\circ})$ grid model using scheme $(hu)_{ppm}$. This represents the most conventional class of schemes that we considered and at a reasonably high resolution. The far-travelled fast waves appear well resolved, coherent and similar in structure to results obtained with the unstructured-model results of Harig et al. (2008). In the shallow-water vicinity of the initial displacement region (centred at $92^{\circ}\text{E}, 7^{\circ}\text{N}$) there is significant noise due to interference of slow short-scale waves and the lack of lateral viscosity. Note that numerical dispersion of the shortest scale waves is expected even though it is physically incorrect. Panel (b) shows the solution from a $30' (\frac{1}{4}^{\circ})$ model using scheme $(hu)_{porous}$, which is a porous wall representation of topography. The immediately obvious differences between the two solutions are due to the inability for the lower resolution model to represent the fine scale waves that are resolved in the higher resolution model. The leading deep-water waves are broadly similar but the coarser resolution is apparent in the lack of sharpness; the wave south of Sri Lanka ($\sim 82^{\circ}\text{E}, 0^{\circ}\text{N}$) is approximately six cells wide (zero crossing-to-zero crossing).

The objective of this study is to establish whether the porous walls allow the leading order effects of fine scale (true) bathymetry to be captured by coarser scale models. We consider the cross-basin travel time of the leading wave front, measured in deep-water to avoid issues with run-up, inundation and shock formation which would mask the deep-water wave travel time. The signal is the average displacement in a $1^{\circ} \times 1^{\circ}$ box centred at $79^{\circ}\text{E}, 4^{\circ}\text{N}$ (indicated by black box in Fig. 13). Averaging over the box permits a sensible comparison between models of different resolutions. We define the arrival time as the time that the spatially averaged displacement reaches half the peak value (timing the position of the peak is less accurate than timing when the signal is changing most rapidly). Fig. 14 shows the arrival time as a function of spatial resolution for the various topographic representations and transport schemes considered.

The first result to note is that all the methods appear to be broadly convergent with resolution. The convergence is for two reasons: the first and most familiar is due to the resolution depen-

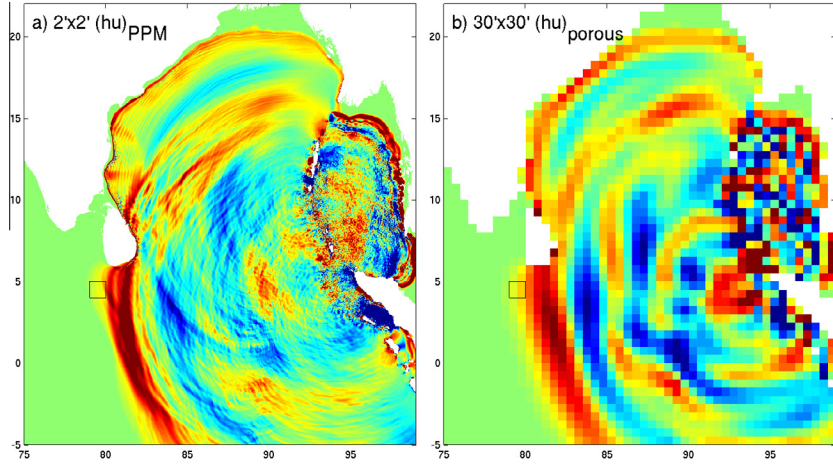


Fig. 13. Sea surface displacement at time 2:20 h after the initial displacements begins (a) in a $2'$ model using conventionally averaged topography and (b) in a $\frac{1}{2}^\circ$ model using the porous-barrier representation. The effect of resolution is obvious in the different scale of resolved waves. The $1' \times 1'$ black square indicates the region of averaging used to measure the cross-basin travel times (covering 30×30 cells and 2×2 cells in the two grids shown). The color-scale range is $\pm \frac{1}{2}$ meters (red positive, blue negative).

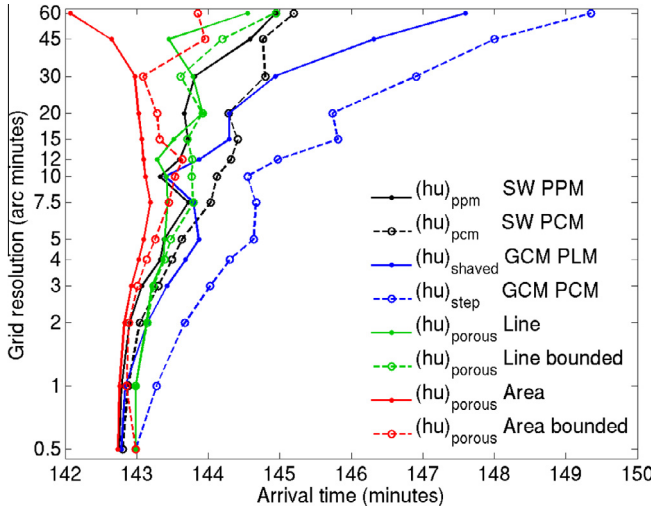


Fig. 14. Arrival time in the $1^\circ \times 1^\circ$ box, indicated in Fig. 13, as a function of spatial resolution for various topographic representations and transport schemes. The travel time is defined as the time when the displacement is half the first peak displacement. The schemes used are defined in Eqs. (7)–(11). For $(hu)_{\text{porous}}$, the labels Line and Area denote different averaging to obtain edge value mean depths. The bounded label indicates that the mean was adjusted to be consistent with the thin-wall connectivity.

dence of spatio-temporal truncation error in the numerically approximated equations. We did not calculate the formal convergence rates due to the mix of schemes between continuity and momentum equations. However, we consider the difference between schemes $(hu)_{\text{ppm}}$ (SW-PPM, black solid) and $(hu)_{\text{pcm}}$ (SW-PCM, black dashed) to be indicative of the traditional truncation errors in a conventional shallow water model. These treatments of thickness transport are considered third and first order accurate respectively, and thus we consider these to be third and first order representations of topography, respectively. The effective depth at a transport point (cell edge) is a function of the sign of the flow and can thus change dramatically from time-step to time-step in regions of large topographic variation.

In contrast to layer models, most general circulation models have a time-invariant effective depth at transport points, as modelled here by schemes $(hu)_{\text{step}}$ and $(hu)_{\text{shaved}}$. The blue curves are thus labelled GCM-PLM ($(hu)_{\text{shaved}}$) and GCM-PCM (for $(hu)_{\text{step}}$)

but both use the exact same topographic data as SW-PPM and SW-PCM. Both the GCM approaches are broadly less accurate than either of the SW schemes (black). The treatment of topography in GCM-PLM is considered second-order accurate but the results appear less accurate than the first-order SW-PCM model. Both GCM-PCM and SW-PCM have first-order treatments of topography but GCM-PCM is significantly less accurate. The difference here can directly be attributed to the static topography component of the thickness flux: because the function PCM is distributive, the scheme $(hu)_{\text{pcm}}$ can be recast as

$$(hu)_{\text{pcm}} = \text{PCM}(u_{i+\frac{1}{2}}, \eta_i) - \text{PCM}(u_{i-\frac{1}{2}}, \bar{D}_i),$$

which differs from scheme $(hu)_{\text{step}}$ only in the second term (the static component). Thus we might conclude that a linear treatment of the static component is less accurate, which is broadly consistent with the preferred use of non-linear limiters in scalar transport. However, we will find that scheme $(hu)_{\text{porous}}$ can be the most accurate even though it also has a linear treatment of the static component.

The green and red lines in Fig. 14 all use the $(hu)_{\text{porous}}$ scheme but we varied the data we used for $\bar{D}_{i+\frac{1}{2}}$. For the green curves we use a linear average, calculated along the cell edge, of topography. This value generally has no contributions from high-resolution topographic data in the interior of the cell. However, for the dashed curve, we adjust the average value to be at or above the thin-wall minimum connectivity calculated in the previous section. The red curves use areal averaging, with a foot-print one half cell on either side of the edge, and the dashed line is similarly bounded by the same thin-wall connectivity.

For the most part, all the porous schemes perform better than the second order GCM scheme, $(hu)_{\text{shaved}}$. The green curves compare well with the third-order SW scheme, $(hu)_{\text{ppm}}$, at coarser resolutions but tend towards the first-order GCM scheme, $(hu)_{\text{step}}$ at finer resolutions. This last result is to be expected at the finest resolution comparable to that of the source topography data. The thin-wall topography interpolation algorithm initializes the thin-wall data on the finest grid using a partial step interpretation of the raw dataset.

The most accurate model is that using the $(hu)_{\text{porous}}$ scheme with areal averages for the edge data. The improvement over using linear average topography can be understood in terms of characteristic solutions; the signal arriving at a point in space integrates the wave speed (ocean depth) along the characteristic path taken.

The areal average approach is more consistent with the characteristic integration along a ray than the linear average which is calculated normal to the transport direction.

The main result we wish to highlight is that, for the most part, the $(hu)_{\text{porous}}$ schemes are less sensitive to resolution than either the layer model (SW) or the GCM style treatments of topography. We consider this evidence that the porous treatment of topography is at least viable, and potentially a more powerful representation of topography than has been used before.

7. Discussion

We have presented a porous media representation of topography as an extension of the cut-cell method that has become widely used in fluid dynamics models and has been implemented in some form in several ocean circulation models. We also presented a thin-wall algorithm for interpolation of high-resolution data onto coarser grids, to generate the data needed to implement a porous media representation of topography in general circulation models.

We demonstrated that the thin-wall interpolation algorithm yields a coarse grid data set that retains overflow sill depths without compromising the topography or barotropic dynamics. We did not evaluate the approach in a three-dimensional general circulation model because it has not yet been implemented. We suggest that models that describe the topography via three-dimensional arrays for face areas and cell volumes could readily adopt the porous media representation. We have not yet considered the consequences for the discretization of terms other than the volume/mass transport.

We could have presented the porous representation of topography as an application of flow through granular materials or porous media. Darcy's law for flow through a porous medium introduces a permeability which essentially modifies the efficiency with which forces can accelerate flow. The resulting scheme might have been similar but understanding how to obtain permeabilities would potentially be more obscure in the context of ocean circulation and topography. The geometric interpretation we presented here, of the sub-grid scale topography and the modulation of transport with elevation, leads to a natural extension of the finite-volume cut-cell method and also allowed us to develop the thin-wall interpolation algorithm.

The thin-wall interpolation algorithm specifically had to consider pathways across quadrilateral cells. A triangular grid approach is conceivable where each triangle is sub-divided into four triangles and might be simpler to develop since there could only be three constraints for three unknowns (edge depths). A more general polygonal grid seems likely to be more challenging to develop.

The added information about topography might be useful for sub-grid scale parametrizations. For instance, the frictional drag on flow should now be aware of the range of topography (as suggested by Robert Hallberg, personal communication). It is also likely that some new parametrizations might be needed if we are to permit large-scale transport via sub-grid scale features. For instance, enhanced diapycnal mixing might be needed to represent the mixing processes in the channels and fissures.

In some models, it is common practice to smooth topography, either for numerical stability or to reduce noise in the solutions. Although we have done nothing to assess the validity of this practice, it is clearly at odds with the approach we present here. Here, we attempted to add more reality to the topography rather than make it less realistic. At first glance it might appear that the more realistic, porous representation of topography will lead to a noisier solution. However, the extra degrees of freedom can introduce a potentially smoother interaction with topography since the trans-

port is no longer abruptly shut-off at a given depth. Instead, the transport gradually reduces with depth as the effective width of the sub-grid scale channels reduce. In essence, the porous representation appears as a smoothing of the vertical position of the rigid boundary and thus we conjecture that it is likely to yield a smoother solution.

Acknowledgements

I would like to thank Sonya Legg for feedback on an early draft of this manuscript, Lucas Harris and Stephen Griffies for internal reviews, as well as two anonymous reviewers for constructive feedback. I also would like to acknowledge the input of many friends and collaborators with whom I have discussed these ideas during the last decade and a half, particularly Arne Biastoch, Chris Hill, Jean-Michel Campin, Martin Losch, Robert Hallberg and Matthew Harrison.

Appendix A. A three parameter curve fit

A truly general and accurate representation of the cumulative pdf, $w(z)$, might be possible but here we suggest a three parameter fit to the data. From the spatial minimum, D_- , spatial maximum, D_+ , and spatial mean, \bar{D} , it is possible to fit a curve that can capture very narrow V-shaped distributions, very broad U-shaped distributions and a smooth range of curves in between. We describe the sorted topography, $D(x)$, on the interval $x \in \{0, \Delta_o\}$ in terms of a non-dimensional curve, $\phi(\chi, m)$ such that

$$D(x) = D_- + (D_+ - D_-)\phi(\chi, m). \quad (\text{A.1})$$

Here $\chi = x/\Delta_o$ is the non-dimensional distance across the element and $m = (\bar{D} - D_-)/(D_+ - D_-)$ is the mean depth normalized by the topographic range. The function $\phi(\chi, m) \in \{0, 1\}$, must be monotonic and exist for $(\chi, m) \in \{0, 1\}$ and have a mean given by $\int_0^1 \phi d\chi = m$. We use the functional form

$$\phi(\chi, m) = \begin{cases} \chi^a & \forall m < \frac{1}{2}, \\ \chi & \text{if } m = \frac{1}{2}, \\ 1 - (1 - \chi)^{1/a} & \forall m > \frac{1}{2}, \end{cases} \quad (\text{A.2})$$

where $a = (1 - m)/m$. One may verify that

$$\begin{aligned} \int_0^{\Delta_o} D(x) dx &= \Delta_o D_- + (D_+ - D_-) \int_0^1 \phi(\chi, m) \frac{dx}{d\chi} d\chi \\ &= \Delta_o (D_- + (D_+ - D_-) m) = \Delta_o \bar{D}. \end{aligned}$$

This description of the distribution $D(x)$ lets us invert for the width of the open segment, $\Delta(z) = \Delta_o w(z)$, as a function of depth, which is defined in terms of the fractional open width, $w(z)$, and in three intervals:

$$w(z) = \begin{cases} 0 & \forall z \leq D_-, \\ \psi(\zeta, m) & \forall D_- \leq z \leq D_+, \\ 1 & \forall z \geq D_+. \end{cases} \quad (\text{A.3})$$

$\psi(\zeta, m)$ is the fractional width in the middle interval and is a monotonic function in the space $(\zeta, m) \in \{0, 1\}$ where $\zeta = (z - D_-)/(D_+ - D_-)$ is a normalized vertical coordinate. $\chi = \psi(\zeta, m)$ is the same curve as $\zeta = \phi(\chi, m)$. Thus

$$\psi(\zeta, m) = \begin{cases} \zeta^{1/a} & \forall m < \frac{1}{2}, \\ \zeta & \text{if } m = \frac{1}{2}, \\ 1 - (1 - \zeta)^a & \forall m > \frac{1}{2}, \end{cases} \quad (\text{A.4})$$

where again $a = (1 - m)/m$.

Eqs. (3) and (4) for the area and volume of fluid below some depth, z , both involve the integral of $w(z)$,

$$\int_{-\infty}^z w(z') dz' = \begin{cases} 0 & \forall z \leq D_-, \\ (D_+ - D_-) \int_0^{z'} \psi(\zeta, m) d\zeta & \forall D_- \leq z \leq D_+, \\ (z - \bar{D}) & \forall z \geq D_+, \end{cases} \quad (\text{A.5})$$

where for the middle interval

$$\int_0^{z'} \psi(\zeta, m) d\zeta = \begin{cases} (1-m)\zeta^{1/(1-m)} & \forall m \leq \frac{1}{2} \\ \frac{1}{2}\zeta^2 & \text{if } m = \frac{1}{2} \\ \zeta - m + m(1-\zeta)^{1/m} & \forall m \geq \frac{1}{2}. \end{cases} \quad (\text{A.6})$$

References

- Adcroft, A., 2013. Thin-wall-topography software suite. <https://github.com/Adcroft/thin-wall-topography>.
- Adcroft, A., Hill, C., Marshall, J., 1997. Representation of topography by shaved cells in a height coordinate ocean model. *Month. Weath. Rev.* 125, 2293–2315. [http://dx.doi.org/10.1175/1520-0493\(1997\)125<2293:ROTBC>2.0.CO;2](http://dx.doi.org/10.1175/1520-0493(1997)125<2293:ROTBC>2.0.CO;2).
- Amante, C., Eakins, B., 2009. ETOPO1 1' Global Relief Model: Procedures, Data Sources and Analysis. Technical report, NOAA Technical Memorandum NESDIS NGDC-24, pp. 19.
- Berger, M., LeVeque, R., 1989. An adaptive cartesian mesh algorithm for the euler equations in arbitrary geometries. AIAA paper 89-1930-CP.
- Colella, P., Woodward, P., 1984. The Piecewise Parabolic Method (PPM) for gas-dynamical simulations. *J. Comp. Phys.* 54, 174–201.
- Ferron, B., Mercier, H., Speer, K., Gargett, A., Polzin, K., 1998. Mixing in the romanche fracture zone. *J. Phys. Oceanogr.* 28, 1929–1945. [http://dx.doi.org/10.1175/1520-0485\(1998\)028<1929:MITRFZ>2.0.CO;2](http://dx.doi.org/10.1175/1520-0485(1998)028<1929:MITRFZ>2.0.CO;2).
- GEBCO, 2010. The GEBCO_08 Grid, version 20100927. <http://www.gebco.net/>.
- Harig, S., Chaeroni, C., Pranowo, W.S., Behrens, J., 2008. Tsunami simulations on several scales: comparison of approaches with unstructured meshes and nested grids. *Ocean Dyn.* 58, 429–440.
- Ingram, D., Causon, D., Mingham, C., 2003. Developments in cartesian cut cell methods. *Math. Comput. Simul.* 61 (3–6), 561–572. [http://dx.doi.org/10.1016/S0378-4754\(02\)00107-6](http://dx.doi.org/10.1016/S0378-4754(02)00107-6).
- Lock, S.-J., Bitzer, H.-W., Coals, A., Gadian, A., Mobbs, S., 2012. Demonstration of a Cut-Cell Representation of 3D Orography for Studies of Atmospheric Flows over Very Steep Hills. *Month. Weath. Rev.* 140(2) pp. 411–424. <http://dx.doi.org/10.1175/MWR-D-11-00069.1>.
- Magaldi, M.G., Haine, T.W.N., Pickart, R.S., 2011. On the Nature and Variability of the East Greenland Spill Jet: A Case Study in Summer 2003. 41:2307–2327. <http://dx.doi.org/10.1175/JPO-D-10-05004.1>.
- Maier-Reimer, E., Mikolajewicz, U., 1992. The Hamburg Large Scale Geostrophic Ocean Circulation Model (Cycle 1). Report No. 2, Max-Planck-Institute für Meteorologie. http://dx.doi.org/10.2312/WDCC/DKRZ_Report_No02.
- Marshall, J., Adcroft, A., Hill, C., Perelman, L., Heisey, C., 1997. A finite-volume, incompressible Navier Stokes model for studies of the ocean on parallel computers. *J. Geophys. Res. Oceans* 102 (C3), 5753–5766.
- NGDC, 2006. ETOPO2v2 Global Gridded 2-minute Database. National Geophysical Data Center, National Oceanic and Atmospheric Administration, U.S. Dept. of Commerce. <http://www.ngdc.noaa.gov/mgg/global/etopo2.html>.
- Pratt, L., Johns, W., Murray, S., Katsumata, K., 1999. Hydraulic Interpretation of Direct Velocity Measurements in the Bab al Mandeb. *J. Phys. Oceanogr.* 29, 2769–2784.
- Price, J., Baringer, M., 1994. Overflows and deep water production by marginal seas. *Prog. Oceanogr.* 33, 161–200.
- Sandwell, D., Wessel, P., 2010. Seamount discovery tool aids navigation to uncharted seafloor features. *Oceanography* 23(1) 34–36.
- Smith, W., Sandwell, D., 1997. Global seafloor topography from satellite and ship depth soundings. *Science* 277, 1957–1962. <http://dx.doi.org/10.1126/science.277.5334.1956>.
- Steppeler, J., Bitzer, H.-W., Minotte, M., and Bonaventura, L. (2002). Nonhydrostatic Atmospheric Modeling using a z-Coordinate Representation. *Mon. Wea. Rev.*, (8):2143–2149. [http://dx.doi.org/10.1175/1520-0493\(2002\)130<2143:NAMUAZ>2.0.CO;2](http://dx.doi.org/10.1175/1520-0493(2002)130<2143:NAMUAZ>2.0.CO;2).
- Werner, F. and Lange, K. (1975). A bathymetric survey of the sill area between the red sea and the gulf of aden. *Geologische Jahrbuch*, 13:125–130.
- Yamazaki, H. and Satomura, T. (2010). Nonhydrostatic Atmospheric Modeling Using a Combined Cartesian Grid. *Mon. Wea. Rev.*, 138(10):3932–3945. <http://dx.doi.org/10.1175/2010MWR3252.1>.